PAPER

Check for updates

Detection of ferrous ions in extracellular vesicles at the single-particle level by nano-flow cytometry

Zuzhe Kang, Chenxi Liu, JunYan Chen, Qiujin Wu, Yunyun Hu, Haonan Di and Xiaomei Yan (ID) *

Iron, particularly redox-active ferrous ions (Fe^{2+}), is essential for biological processes. Despite their pivotal roles, analysis of Fe^{2+} ions within individual extracellular vesicles (EVs) has been hindered by the ultralow Fe^{2+} content and substantial heterogeneity of EVs. To address this, we developed a novel approach by integrating an Fe^{2+}-specific fluorescent chemosensor (**Ac-FluNox**) with nano-flow cytometry (nFCM) for precise single-EV Fe^{2+} mapping. Method specificity to Fe^{2+} was validated *via* Fe^{2+}-loaded liposomal models at the single-particle level. Comprehensive profiling of Fe^{2+} distributions in HT-1080-derived EVs under varying ferroptotic stress conditions revealed the striking heterogeneity in Fe^{2+} loading among EVs and a strong positive correlation between EV Fe^{2+} levels and their parental cells. Notably, we identified an EV-mediated Fe^{2+} export mechanism that functionally parallels to ferroportin (FPN)-dependent iron efflux, suggesting EVs may serve as a compensatory iron-release pathway during FPN inhibition. The nFCM platform achieved superior detection sensitivity with high throughput (up to 10^4 particles per min), providing a powerful analytical tool for investigating EV heterogeneity and Fe^{2+}-mediated regulatory networks in iron homeostasis and ferroptosis-related pathologies.

Introduction

Iron, the most abundant transition metal in human physiology, serves as a pivotal redox cofactor in oxygen-dependent metabolic pathways, spanning mitochondrial respiration, hemoglobin-mediated oxygen transport, and ATP synthesis, mediated by its unique electron-shutting capacity *via* Fe^{2+}/Fe^{3+} interconversion.[1–3] Cellular ion homeostasis is precisely controlled by iron-regulatory proteins that maintain the dynamic equilibrium between Fe^{2+} and Fe^{3+}.[4–6] Due to the high cellular abundance of reductants such as glutathione, intracellular labile iron consists of Fe^{2+} primarily, which participates in regulating iron metabolism through binding to small molecules or proteins.[7–9] Therefore, elucidating Fe^{2+}-mediated regulatory mechanisms provides critical insights into metabolic homeostasis and iron-regulatory networks. Although cells have evolved sophisticated systems for the uptake, transport, utilization, storage, and export of Fe^{2+},[10–12] the intricacies of intercellular Fe^{2+} regulation remain poorly understood.[13–15] Extracellular vesicles (EVs), nanoscale lipid-bilayer-delimited particles that mediate intercellular communication through selective cargo transfer,[16–18] have emerged as key players in iron-related bioactive substance trafficking.[2,19,20] The biogenesis of Fe^{2+}-containing EVs occurs through coordinated interactions between multiple organelles (including endosomes, lysosomes, and mitochondria) and cytosolic Fe^{2+} pools, enabling active loading of redox-active iron during vesicle maturation. Through this mechanism, EVs critically regulate parental cell iron homeostasis and ferroptosis propagation.[13,14,21] Consequently, quantification of intravesicular Fe^{2+} is indispensable for deciphering EV-mediated biological functions and their underlying regulatory networks.

Iron exhibits diverse chemical speciation and functional states within EVs, encompassing free Fe^{2+}, Fe^{3+}, and ferritin-bound iron.[2] While inductively coupled plasma mass spectrometry (ICP-MS) has enabled quantification of total iron content in EVs, this approach lacks specificity for discriminating between distinct iron species.[22] Current methodologies, including advanced fluorescent chemosensors and commercial assay kits, require EV disruption for Fe^{2+} detection,[23,24] thereby providing only ensemble-averaged measurements that obscure the inherent heterogeneity of EVs. Single-EV characterization technologies, such as super-resolution fluorescence microscopy, droplet digital PCR (ddPCR), and nano-flow cytometry (nFCM), have unequivocally demonstrated the marked heterogeneity of EVs in terms of size, composition, and cargo loading.[25–29] Consequently,

Department of Chemical Biology, MOE Key Laboratory of Spectrochemical Analysis & Instrumentation, Key Laboratory for Chemical Biology of Fujian Province, State Key Laboratory of Physical Chemistry of Solid Surfaces, College of Chemistry and Chemical Engineering, Xiamen University, Xiamen 361005, Fujian, China. E-mail: xmyan@xmu.edu.cn
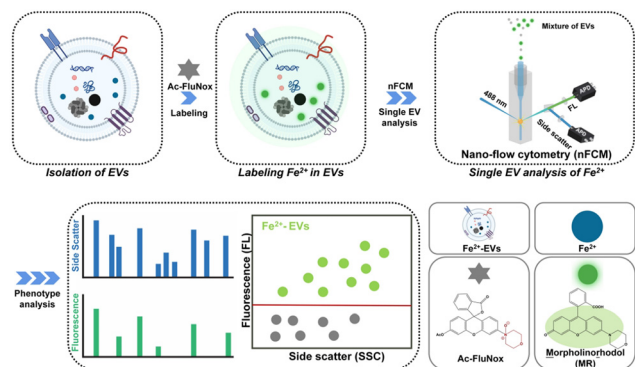
Scheme 1 Single-EV Fe^{2+} profiling *via* **Ac-FluNox** labeling coupled with nFCM detection.

single-particle-resolution analysis of Fe^{2+} within EVs represents a fundamental prerequisite for investigating the heterogeneity and regulatory mechanisms of EVs in iron metabolism. Building on these technological advances, nFCM stands out as the optimal platform for single-EV Fe^{2+} analysis, uniquely combining: (i) high-throughput detection (up to 10^4 particles per min) essential for capturing population heterogeneity; (ii) quantitative multiparameter measurement of size, fluorescence intensity, and concentration; and (iii) sizing accuracy comparable to cryo-TEM, which collectively enabling unprecedented resolution of Fe^{2+} distribution patterns in EV subpopulations.[30,31]

In this study, we developed a novel method for detecting Fe^{2+} in individual EVs by integrating the Fe^{2+}-specific fluorescent chemosensor (**Ac-FluNox**) with nFCM (Scheme 1).

Upon esterase activation within EVs, **Ac-FluNox** generated morpholinorhodol (MR) through its reaction with Fe^{2+}, exhibiting detectable green fluorescence. The specificity and reliability of this Fe^{2+} labeling approach were validated using Fe^{2+}-loaded liposomes as model systems. Leveraging this platform, we performed systematic profiling of Fe^{2+} distributions and dynamic changes in EVs derived from HT-1080 cells under various ferroptosis-inducing conditions. Significantly, our results revealed a strong correlation of Fe^{2+} levels between EVs and their parental cells, providing mechanistic insights into EV-mediated regulation of iron homeostasis during ferroptosis.

Results and discussion

Synthesis and performance evaluation of Fe^{2+} chemosensor Ac-FluNox

As illustrated in Scheme S1, the fluorescent chemosensor **Ac-FluNox** was synthesized according to the previously reported procedure,[32,33] with the target compound characterized by ^{1}H NMR, ^{13}C NMR (Fig. S1 and S2). Leveraging N-oxide chemistry for fluorescence switching, the N–O bond in **Ac-FluNox** isolates the nitrogen atom from p-conjugation, yielding a fluorescence turn-off state. Subsequential esterase hydrolysis followed by Fe^{2+}-mediated deoxygenation converts **Ac-FluNox** to morpholinorhodol (MR), which exhibits strong green fluorescence (Fig. 1a). Owing to its inherent lipophilicity, **Ac-FluNox** readily traverses lipid bilayers *via* passive diffusion, achieving efficient loading into both
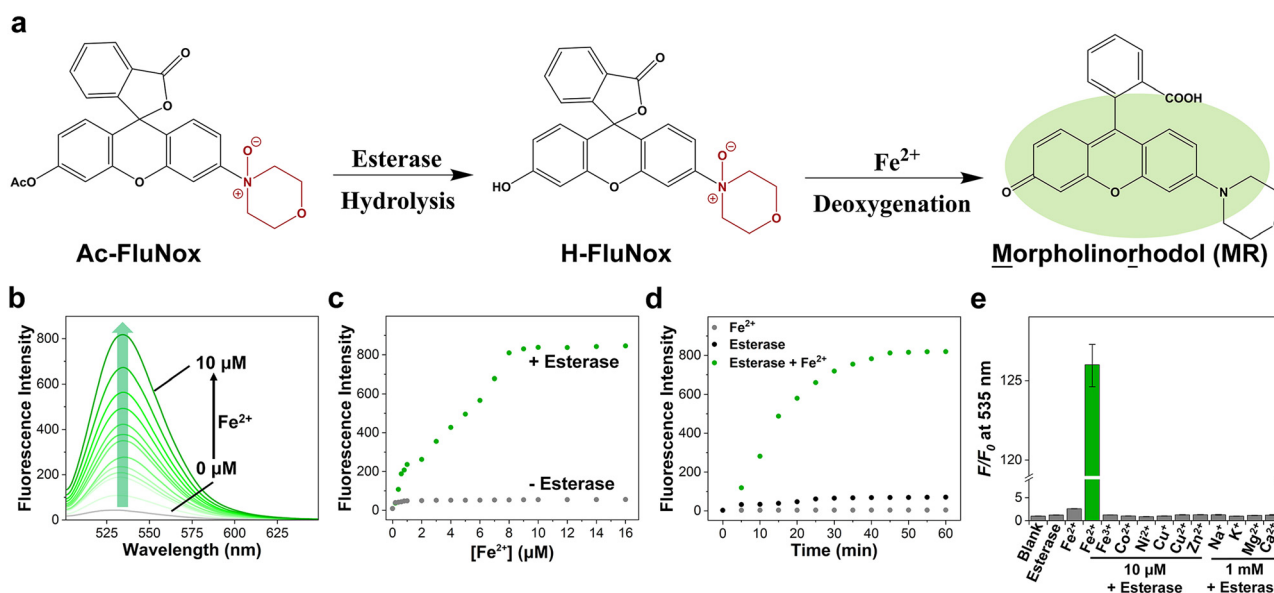
Fig. 1 Fluorescence responses of **Ac-FluNox** for Fe^{2+} detection in HEPES buffer (50 mM, pH 7.4, 0.2% DMSO). (a) The mechanism of Fe^{2+}-specific fluorescence activation of **Ac-FluNox** *via* sequential esterase-catalyzed hydrolysis (generating **H-FluNox**) and Fe^{2+}-mediated deoxygenation to yield morpholinorhodol (**MR**), a green-emitting fluorophore. (b) Fluorescence emission spectra of **Ac-FluNox** (1.0 μM) upon reaction with different concentrations of Fe^{2+} (0–10 μM) in the presence of esterase (0.1 mg mL^{-1}). (c) Dose–response curves of **Ac-FluNox** (1.0 μM) fluorescence intensity (l_{em} = 535 nm) with increasing Fe^{2+} (0–16 μM), with or without of esterase (0.1 mg mL^{-1}). (d) Time-dependent fluorescence enhancement (recorded at 5 min intervals) of **Ac-FluNox** (1.0 μM) upon addition of Fe^{2+} (10 μM) in the presence of esterase (0.1 mg mL^{-1}). (e) Metal selectivity test against various metal ions. The error bar represents the standard deviation (s.d.) of three replicate experiments (n = 3, mean ± s.d.).

natural EV membranes and artificial liposomes. This dual-enzyme/metal-responsive mechanism establishes **Ac-FluNox** as a promising probe for Fe^{2+} detection in EVs *via* nFCM.

The fluorescence response of **Ac-FluNox** was systematically evaluated for Fe^{2+} sensing in HEPES buffer containing esterase (0.1 mg mL^{-1}). Upon gradual increase of Fe^{2+} (0–10 μM), a 75.2-fold fluorescence enhancement in green fluorescence emission (λ_{ex} = 490 nm, λ_{em} = 535 nm) was observed at 10 μM Fe^{2+} within 60 min (Fig. 1b–d), demonstrating rapid and efficient Fe^{2+} detection, a feature that leverages the ubiquitous presence of esterase in EVs for precise intravesicular Fe^{2+} analysis.[34,35] Furthermore, the selectivity of **Ac-FluNox** for Fe^{2+} was investigated. As demonstrated in Fig. 1e, negligible fluorescence was observed in the presence of biologically relevant interferents, confirming the probe's specificity and stability for Fe^{2+} detection in complex biological environments. Collectively, these results rigorously validated that **Ac-FluNox** not only quantitatively detects Fe^{2+} in solutions, but also serves as a highly selective sensor for monitoring Fe^{2+} changes.

Single-liposome Fe^{2+} profiling

To validate the single-particle Fe^{2+} labeling method, we synthesized liposomes (LPs) encapsulating Fe^{2+} (0–4.0 μM) and esterase (0.1 mg mL^{-1}) *via* microfluidics (Fig. 2a(i) and b). During microfluidic assembly, Fe^{2+} and esterase were successfully co-encapsulated within the liposomes' aqueous lumen, leveraging their characteristic phospholipid bilayer-enclosed aqueous core architecture (Fig. 2b). The liposomes were stained with **Ac-FluNox** and analyzed by nFCM. Analysis of liposome size distribution following refractive index correction using Mie theory revealed that variations in encapsulated Fe^{2+} concentration had negligible effects on particle size distribution (Fig. S3 and S4). The observed heterogeneity in size and fluorescence distributions reflects the size-dependent loading variability inherent to liposome

populations (Fig. 2a(ii)). Both the percentage ratio and median FL intensity of Fe^{2+}-positive-liposomes (Fe^{2+}-LPs) showed concentration-dependent responses to Fe^{2+} (Fig. 2c and d). The strong linear correlation (R^2 = 0.9812) between Fe^{2+}-LPs' median FL intensity and Fe^{2+} loading concentration demonstrates **Ac-FluNox**'s capability for quantifying Fe^{2+} in single particles *via* nFCM (Fig. 2d). These results establish the nFCM-based single-particle Fe^{2+} detection method as a robust platform for intravesicular Fe^{2+} analysis with direct applicability to EV studies.

### Property characterization of EVs derived from ferroptotic cells

The nFCM-based single-particle Fe^{2+} detection method was applied to analyze EVs derived from HT-1080 cells, a well-established human fibrosarcoma cell line for ferroptosis research. EVs were isolated through sequential centrifugation (1000g, 5 min; 2000g, 10 min) and ultracentrifugation (100 000g, 2 h, twice) (Fig. 3a). TEM imaging confirmed typical EV morphology (Fig. 3b and S5), while Western blotting verified the presence of classical EV markers CD9 and TSG101 and the absence of the endoplasmic reticulum (ER) marker calnexin in the EV preparation (Fig. 3c). Triton X-100 treatment, developed in our previous study,[31,36] was conducted, affirming a purity (defined as the detergent sensitivity) of 88.6% for the HT-1080 EVs isolate (Fig. 3d).

Three ferroptosis inducers were used to treat HT-1080 cells: ammonium ferric citrate (FAC, 0–200 μg mL^{-1}), RSL3 (0–2 μM), and erastin (0–4 μM). FAC serves as a direct iron source that elevates intracellular labile iron pool (LIP) levels through cellular uptake and subsequent reduction.[2,37] Both RSL3 and erastin are classical ferroptosis inducers that indirectly increase intracellular Fe^{2+} levels through promoting ferritin degradation, RSL3 through GPX4 inhibition and erastin *via* system x_c^- blockade.[1] All treatments (48 h incubation) maintained >80% cell viability (Fig. S6). Iron
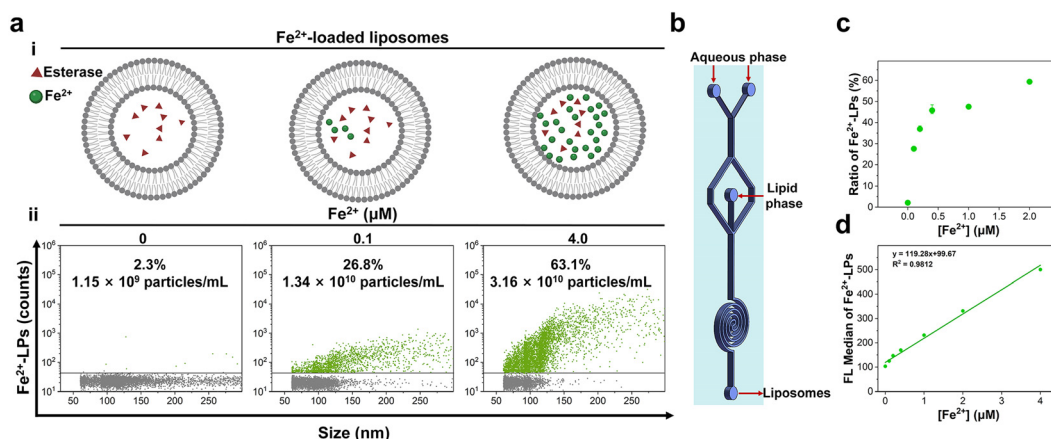
Fig. 2 Analysis of Fe^{2+} in individual Fe^{2+}-encapsulated liposomes using nFCM. (a) Schematic diagram of liposome formulations with graded Fe^{2+} concentrations (0–4.0 μM) (i) and representative bivariate dot-plots of Fe^{2+} fluorescence (FL) *versus* particle size for liposomes labeled with **Ac-FluNox** (ii). (b) Microfluidic device schematic for liposomes synthesis. (c) Scatter plot presenting percentage ratios of Fe^{2+}-LPs. (d) Linear regression correlating FL median with intra-liposomal Fe^{2+} concentration. Initial concentration of liposome: ~5.0 × 10^{10} particles per mL. The concentrations of Fe^{2+}-LPs were calculated by multiplying the positive ratios with the initial liposome concentration. Error bars represent standard deviation (s.d.) of three replicate experiments (n = 3, mean ± s.d.).
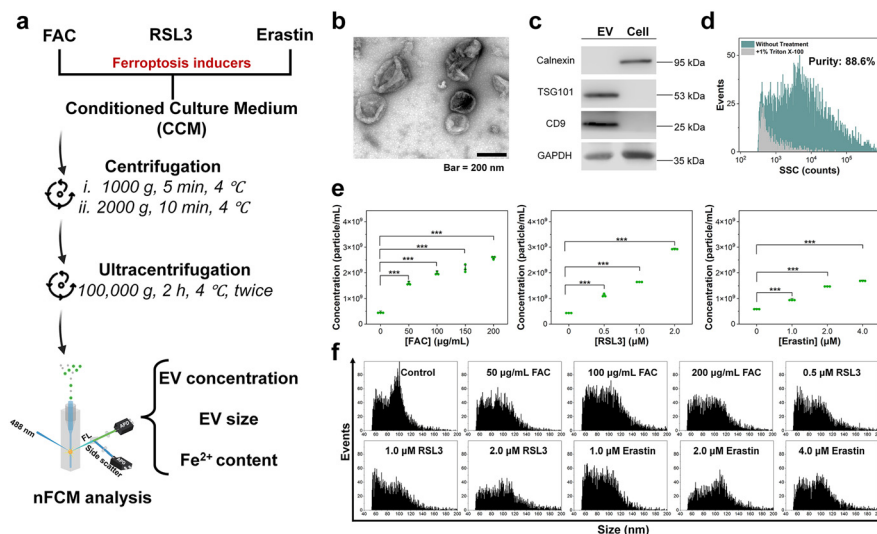
Fig. 3 Characterization of EVs released during ferroptosis. (a) Workflow of EV isolation and purification from HT-1080 cells. (b) Representative TEM micrograph of EVs isolated from the conditioned cell culture medium (CCCM) of untreated HT-1080 cells. (c) Immunoblots comparing a cell lysate with an EV preparation (10 μg protein per lane). (d) Side scatter (SSC) distribution histograms of EVs before and after Triton X-100 treatment. (e) Quantitative comparison of secreted particle concentration of EVs under different treatment conditions in per mL of conditioned medium. (f) Comparison of EV size distribution under different treatment conditions. Error bars represent the standard deviation (s.d.) of three replicate experiments (n = 3, mean ± s.d.).

overload conditions significantly enhanced EV secretion (Fig. 3e), suggesting a stress-responsive regulatory mechanism in parental cells. Notably, all EV populations exhibited similar size distributions (Fig. 3f), confirming the preservation of EV integrity under different iron metabolic states. Taken together, the isolated EVs met all quality criteria for subsequent Fe^{2+} profiling.

Single-particle analysis of Fe^{2+} in EVs during ferroptosis *via* nFCM

Previous studies have established the association between Fe^{2+} fluctuations and ferroptosis, with distinct cellular Fe^{2+} levels observed across different induction pathways.[1] However, whether ferroptosis drives Fe^{2+} accumulation in
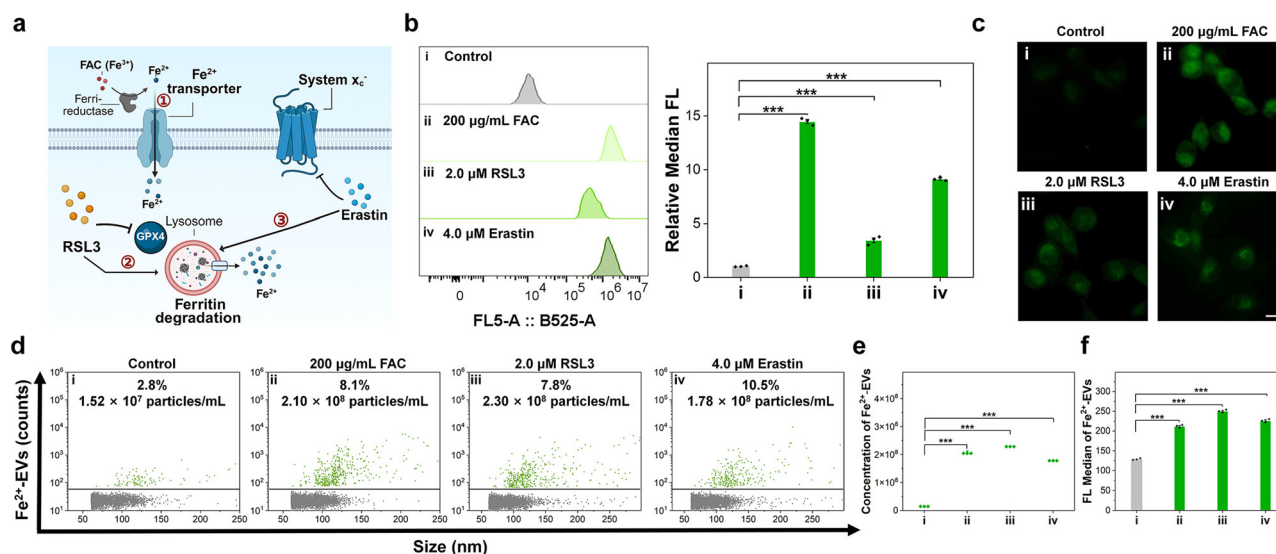
Fig. 4 Analysis of Fe^{2+} in EVs derived from ferroptotic HT-1080 cells treated with different ferroptosis inducers. (a) Schematic diagram of the regulatory mechanisms of FAC, RSL3, and erastin on iron metabolism. (b) Fe^{2+} level in HT-1080 cells treated with different inducers by flow cytometric analysis. (c) Confocal microscope images of **Ac-FluNox**-stained HT-1080 cells treated with different inducers. (d) Bivariate dot-plots of FL *versus* particle size of EVs derived from different treatments. (e) Absolute concentrations of Fe^{2+}-positive EVs calculated by multiplying the positive ratios from panel (d) with corresponding total particle concentrations. (f) Bar graphs presenting FL median of Fe^{2+} positive EVs in (d). The labels i–iv represent different treatments (i: control, ii: 200 μg mL^{-1} FAC, iii: 2.0 μM RSL3, and iv: 2.0 μM erastin). Scale bar: 20 μm. The error bar represents the standard deviation (s.d.) of three replicate experiments (n = 3, mean ± s.d.).

EVs, and whether EVs serves as an iron export mechanism parallel to ferroportin FPN, remains unclear. Capitalizing on the single-particle resolution of nFCM for intravesicular Fe^{2+} analysis, we performed quantitative mapping of Fe^{2+} in individual EVs. Initial investigations focused on FAC-induced iron overload (Fig. 4a). Flow cytometry and confocal microscopy confirmed dose-dependent intracellular Fe^{2+} accumulation in HT-1080 cells after 48-hour FAC treatment (Fig. 4b and c and S7). To compare the correlation between parental cells and EVs in Fe^{2+} content, **Ac-FluNox** was used to label Fe^{2+} in EVs. nFCM analysis revealed FAC concentration-dependent increases in Fe^{2+}-positive EV ratios and their median fluorescence intensity, which were attenuated by the iron chelator deferoxamine (DFO), confirming the iron-dependent nature of these responses (Fig. S8). These results, combined with the FAC-induced increase in EV secretion

(Fig. 3e) demonstrate synchronized intracellular–extracellular Fe^{2+} dynamics, suggesting a regulatory link between cellular iron status and EV biogenesis.

We extended these observations to ferroptosis inducers that indirectly alter iron homeostasis through promoting ferritin degradation (Fig. 4a). Flow cytometry and fluorescence microscopy imaging (Fig. 4b and c) demonstrated RSL3- and erastin-induced iron overload in HT-1080 cells, mediated by ferritin degradation followed by Fe^{3+} release and reduction. EVs generated under ferroptosis induction exhibited Fe^{2+} accumulation patterns similar to those of FAC-treated EVs (Fig. 4b–f and S8), with increases in both particle concentration and median fluorescence intensity of Fe^{2+}-positive populations. Together, these results demonstrate that iron-overloaded cells actively release Fe^{2+}-enriched EVs, with their Fe^{2+} content closely linked to
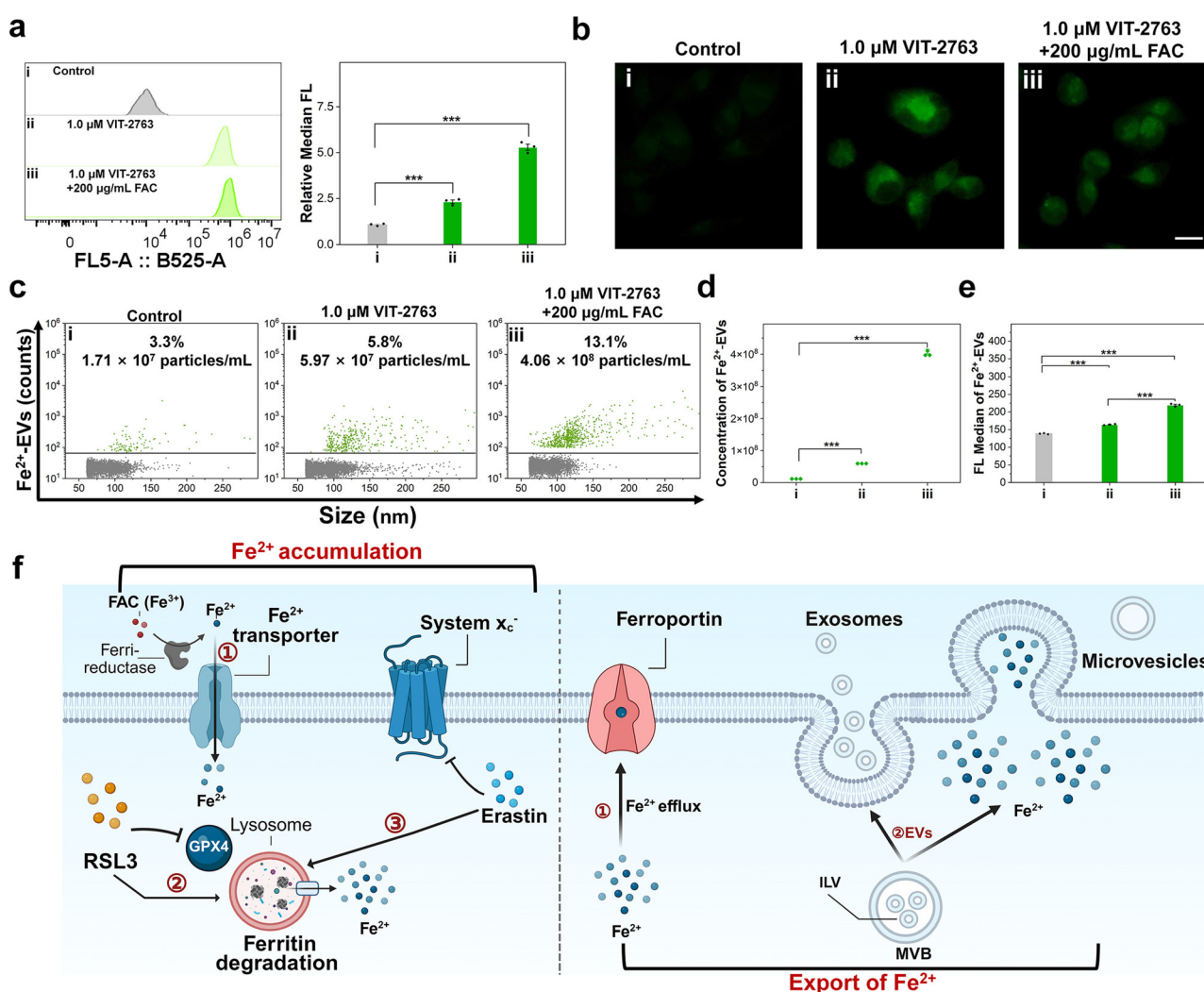
Fig. 5 Analysis of Fe^{2+} in EVs derived from ferroptotic HT-1080 cells under FPN inhibition. (a and b) Flow cytometric analysis (a) and confocal microscope images (b) of intracellular Fe^{2+} level in HT-1080 cells treated with different conditions upon **Ac-FluNox** staining. (c) Bivariate dot-plots of FL *versus* particle size of Fe^{2+}-EVs derived from different treatments. (d and e) Bar graphs of the particle concentration (d) and FL median intensity (e) of Fe^{2+}-EVs in (c). Scale bar: 20 μm. (f) Schematic diagram of the dual-phase iron export systems. The labels i–iii represent different treatments (i: control, ii: 1.0 μM VIT-2763, and iii: 1.0 μM VIT-2763 + 200 μg mL^{-1} FAC). The error bar represents the standard deviation (s.d.) of three replicate experiments (n = 3, mean ± s.d.).

parental cell iron metabolism—supporting the involvement of an active transport process.

Exploring the relationship between FPN and EVs in Fe^{2+} export

Building on nFCM evidence of EV-mediated iron homeostasis regulation during stress (Fig. 4b–f and S8), we postulated that EVs might functionally compensate for FPN deficiency by providing an alternative Fe^{2+} efflux pathway. To test this, we employed VIT-2763, a specific FPN inhibitor, to pharmacologically block canonical iron efflux.[38] Consistent with FPN inhibition, quantitative analysis revealed significant intracellular Fe^{2+} accumulation in HT-1080 cells (Fig. 5a and b), while parallel detection of EV-associated Fe^{2+} confirmed compensatory extracellular export (Fig. 5c–e). Notably, under combined FPN inhibition and iron overload induced by FAC, RSL3, or erastin, elevated particle concentrations and Fe^{2+} FL intensities of Fe^{2+}-EVs were observed (Fig. 5c–e, S9 and S10). These results further demonstrate that EV-mediated Fe^{2+} export increases proportionally with both pharmacological FPN inhibition and pathological iron overload. Collectively, these findings establish a dual-phase iron export system wherein iron-overloaded cells not only export Fe^{2+} *via* FPN but also release Fe^{2+} into the extracellular microenvironment in an EV-dependent manner. Importantly, EV-mediated efflux is further activated as an adaptive response to FPN dysfunction (Fig. 5f schematic). This spontaneous compensatory mechanism likely represents a cellular safeguard against iron toxicity when FNP-meditated export pathway is compromised.

Conclusions

In conclusion, this study elucidates the regulatory role of EVs in iron homeostasis, with specific focus on Fe^{2+}. By developing a novel analytical platform combining Fe^{2+}-specific fluorescent chemosensor (**Ac-FluNox**) with nFCM, we achieved single-EV resolution for quantitative Fe^{2+} characterization. This approach enabled the precise characterization of Fe^{2+} distribution and content in EVs, revealing a strong correlation between Fe^{2+} levels in EVs and their parental cells. Moreover, we discovered the capacity of EVs to function as an auxiliary Fe^{2+} export system complementing FPN-mediated efflux. This study not only advances the understanding of iron regulatory networks by demonstrating EV-mediated Fe^{2+} transport but also establishes a versatile platform for investigating the heterogeneity and functional significance of EVs in iron metabolism and associated pathological conditions. While the current methodology specifically detects free Fe^{2+}, future studies incorporating nFCM's multiparametric capabilities could extend to iron-containing cargos (*e.g.*, ferritin), offering more comprehensive insights into EV-mediated iron communication. This direction would further unravel the multifaceted roles of EVs in iron regulation under physiological and pathological conditions.

Conflicts of interest

The authors declare the following competing financial interest(s): X. Y. declares competing financial interest as a cofounder of NanoFCM Inc., a company committed to commercializing the nano-flow cytometry (nFCM) technology.

Data availability

Supplementary information is available: Including experimental details and supplementary results. See DOI: **https://doi.org/10.1039/D5SD00060B.**

The data supporting this article have been included as part of the SI.

Acknowledgements

References

1 S. J. Dixon and J. A. Olzmann, *Nat. Rev. Mol. Cell Biol.*, 2024, **25**, 424–442.

2 B. Galy, M. Conrad and M. Muckenthaler, *Nat. Rev. Mol. Cell Biol.*, 2024, **25**, 133–155.

3 K. B. Muchowska, S. J. Varma and J. Moran, *Nature*, 2019, **569**, 104–107.

4 M. W. Hentze, M. U. Muckenthaler, B. Galy and C. Camaschella, *Cell*, 2010, **142**, 24–38.

5 P. Matak, A. Matak, S. Moustafa, D. K. Aryal, E. J. Benner, W. Wetsel and N. C. Andrews, *Proc. Natl. Acad. Sci. U. S. A.*, 2016, **113**, 3428–3435.

6 F. X. Sun, Z. Z. Zhao, M. M. Willoughby, S. Q. Shen, Y. Zhou, Y. Y. Shao, J. Kang, Y. T. Chen, M. Y. Chen, X. J. Yuan, I. Hamza, A. R. Reddi and C. Y. Chen, *Nature*, 2022, **610**, 768–774.

7 K. Kawai, T. Hirayama, H. Imai, T. Murakami, M. Inden, I. Hozumi and H. Nagasawa, *J. Am. Chem. Soc.*, 2022, **144**, 3793–3803.

8 R. C. Hider and X. L. Kong, *BioMetals*, 2011, **24**, 1179–1187.

9 S. J. Patel, A. G. Frey, D. J. Palenchar, S. Achar, K. Z. Bullough, A. Vashisht, J. A. Wohlschlegel and C. C. Philpott, *Nat. Chem. Biol.*, 2019, **15**, 872–881.

10 L. C. Montemiglio, C. Testi, P. Ceci, E. Falvo, M. Pitea, C. Savino, A. Arcovito, G. Peruzzi, P. Baiocco, F. Mancia, A. Boffi, A. d. Georges and B. Vallone, *Nat. Commun.*, 2019, **10**, 1121.

11 J. Gruszczyk, U. Kanjee, L. J. Chan, S. Menant, B. Malleret, N. T. Y. Lim, C. Q. Schmidt, Y. F. Mok, K. M. Lin, R. D. Pearson, G. Rangel, B. J. Smith, M. J. Call, M. P. Weekes, M. D. W. Griffin, J. M. Murphy, J. Abraham, K. Sriprawat, M. J. Menezes, M. U. Ferreira, B. Russell, L. Renia, M. T. Duraisingh and W. H. Tham, *Science*, 2018, **359**, 48–55.

12 H. H. Jabara, S. E. Boyden, J. Chou, N. Ramesh, M. J. Massaad, H. Benson, W. Bainter, D. Fraulino, F. Rahimov, C.

Sieff, Z. J. Liu, S. H. Alshemmari, B. K. Al-Ramadi, H. Al-Dhekri, R. Arnaout, M. Abu-Shukair, A. Vatsayan, E. Silver, S. Ahuja, E. G. Davies, M. Sola-Visner, T. K. Ohsumi, N. C. Andrews, L. D. Notarangelo, M. D. Fleming, W. Al-Herz, L. M. Kunkel and R. S. Geha, *Nat. Genet.*, 2016, **48**, 74–78.

13 I. Yanatori, D. R. Richardson, H. S. Dhekne, S. Toyokuni and F. Kishi, *Blood*, 2021, **138**, 1490–1503.

14 C. W. Brown, J. J. Amante, P. Chhoy, A. L. Elaimy, H. Liu, L. J. Zhu, C. E. Baer, S. J. Dixon and A. M. Mercurio, *Dev. Cell*, 2019, **51**, 575–586.

15 M. Truman-Rosentsvit, D. Berenbaum, L. Spektor, L. A. Cohen, S. Belizowsky-Moshe, L. Lifshitz, J. Ma, W. Li, E. Kesselman, I. Abutbul-Ionita, D. Danino, L. Gutierrez, H. H. Li, K. Y. Li, H. F. Lou, M. Regoni, M. Poli, F. Glaser, T. A. Rouault and E. G. Meyron-Holtz, *Blood*, 2018, **131**, 342–352.

16 R. Kalluri and V. S. LeBleu, *Science*, 2020, **367**, 640.

17 M. Tkach and C. Théry, *Cell*, 2016, **164**, 1226–1232.

18 G. van Niel, G. D'Angelo and G. Raposo, *Nat. Rev. Mol. Cell Biol.*, 2018, **19**, 213–228.

19 G. S. Bi, J. Q. Liang, Y. Y. Bian, G. Y. Shan, Y. W. Huang, T. Lu, H. Zhang, X. Jin, Z. C. Chen, M. N. Zhao, H. Fan, Q. Wang, B. Y. Gan and C. Zhan, *Nat. Commun.*, 2024, **15**, 2461.

20 C. W. Brown and A. M. Mercurio, *Mol. Cell. Oncol.*, 2020, **7**, e1730144.

21 H. K. C. Co, C. C. Wu, Y. C. Lee and S. H. Chen, *Nature*, 2024, **631**, 654–662.

22 A. Purnianto, C. Mawal, M. M. Kulkarni, H. Su, T. F. Koukoulis, P. Wongsodirdjo, Y. H. Hung, S. Ayton, A. I. Bush, K. J. Barnham and L. J. Vella, *J. Extracell. Biol.*, 2024, **3**, e70012.

23 C. Alarcón-Veleiro, R. Mato-Basalo, S. Lucio-Gallego, A. Vidal-Pampín, M. Quindós-Varela, T. Al-Qatarneh, G. Berrecoso, A. Vizoso-Vázquez, M. C. Arufe and J. Fafián-Labora, *Antioxidants*, 2023, **12**, 183.

24 K. Grover, A. Koblova, A. T. Pezacki, C. J. Chang and E. J. New, *Chem. Rev.*, 2024, **124**, 5846–5929.

25 K. Lee, K. Fraser, B. Ghaddar, K. Yang, E. Kim, L. Balaj, E. A. Chiocca, X. O. Breakefield, H. Lee and R. Weissleder, *ACS Nano*, 2018, **12**, 494–503.

26 Y. N. Guo, J. Tao, Y. R. Li, Y. M. Feng, H. X. Ju, Z. F. Wang and L. Ding, *J. Am. Chem. Soc.*, 2020, **142**, 7404–7412.

27 J. L. Zhang, J. J. Shi, H. L. Zhang, Y. F. Zhu, W. Liu, K. X. Zhang and Z. Z. Zhang, *J. Extracell. Vesicles*, 2020, **10**, e12025.

28 B. Q. Lin, T. Tian, Y. Z. Lu, D. Liu, M. J. Huang, L. Zhu, Z. Zhu, Y. L. Song and C. Y. Yang, *Angew. Chem., Int. Ed.*, 2021, **60**, 7582–7586.

29 H. S. Liu, Y. Tian, C. F. Xue, Q. Niu, C. Chen and X. M. Yan, *J. Extracell. Vesicles*, 2022, **11**, e12206.

30 S. B. Zhu, L. Ma, S. Wang, C. X. Chen, W. Q. Zhang, L. L. Yang, W. Hang, J. P. Nolan, L. N. Wu and X. M. Yan, *ACS Nano*, 2014, **8**, 10998–11006.

31 Y. Tian, L. Ma, M. F. Gong, G. Q. Su, S. B. Zhu, W. Q. Zhang, S. Wang, Z. B. Li, C. X. Chen, L. H. Li, L. N. Wu and X. M. Yan, *ACS Nano*, 2018, **12**, 671–680.

32 T. Peng and D. Yang, *Org. Lett.*, 2010, **12**, 496–499.

33 T. Hirayama, H. Tsuboi, M. Niwa, A. Miki, S. Kadota, Y. Ikeshita, K. Okuda and H. Nagasawa, *Chem. Sci.*, 2017, **8**, 4858–4866.

34 G. Adamo, S. Picciotto, P. Gargano, A. Paterna, S. Raccosta, E. Rao, D. P. Romancino, G. Ghersi, M. Manno, M. Salamone and A. Bongiovanni, *J. Extracell. Vesicles*, 2025, **14**, e70030.

35 K. Wardhani, A. Levina, G. E. R. Grau and P. A. Lay, *Chem. Soc. Rev.*, 2024, **53**, 6779–6829.

36 N. G. Cai, X. Z. Zhan, Y. Chen, J. W. Xue, C. Chen, Y. R. Li, Y. Tian and X. M. Yan, *Anal. Chem.*, 2024, **96**, 12718–12728.

37 J. A. Pan, W. Y. Xiong, A. L. Zhang, H. Zhang, H. Lin, L. Gao, J. H. Ke, S. Y. Huang, J. F. Zhang, J. Gu, A. C. Y. Chang and C. Q. Wang, *Adv. Sci.*, 2023, **10**, 2206007.

38 V. Manolova, N. Nyffenegger, A. Flace, P. Altermatt, A. Varol, C. Doucerain, H. Sundstrom and F. Dürrenberger, *J. Clin. Invest.*, 2020, **130**, 491–506.